Vertical mixing derived from surface chlorophyll-a concentrations of the North Atlantic ocean

Article *in* Journal of Atmospheric and Oceanic Technology · July 2016

DOI: 10.1175/JTECH-D-16-0053.1

3 authors, including:

Lisa Hahn-Woernle
University of Hawai'i at Mānoa
9 PUBLICATIONS **152** CITATIONS
SEE PROFILE

Hans J Van Der Woerd
VU University Amsterdam
131 PUBLICATIONS **1,007** CITATIONS
SEE PROFILE

Vertical Mixing Derived from Surface Chlorophyll-*a* Concentrations of the North Atlantic Ocean

LISA HAHN-WOERNLE AND HENK A. DIJKSTRA

Institute for Marine and Atmospheric Research Utrecht (IMAU), Utrecht, Netherlands

HANS J. VAN DER WOERD

Institute for Environmental Studies (IVM), Free University of Amsterdam, Amsterdam, Netherlands

(Manuscript received 22 February 2016, in final form 29 June 2016)

ABSTRACT

Vertical mixing is thought to play an essential role in phytoplankton blooms, yet measurements of mixing properties are very sparse. This paper presents a methodology to estimate profiles of the upper-ocean vertical mixing from satellite color observations, using a coupled turbulence–phytoplankton model and data assimilation–based calibration techniques. The method is tested at a location in the eastern North Atlantic for which an integrated set of observations (vertical mixing, phytoplankton, nutrients) is available. Results of identical twin experiments show that the method is very robust and achieves accurate turbulence model parameter calibrations even with noisy or sparsely sampled observations. The application of surface chlorophyll-*a* (Chl *a*) concentration to MODIS *Aqua* satellite observations leads two independent cases (data for the years 2009 and 2011) to a calibration of the model parameterization that produces weaker winter mixing compared to the standard configuration. As a consequence of the weaker mixing, the timing and intensity of increased surface Chl *a* satellite observations in spring and summer was reproduced by the model. Moreover, the weaker mixing resembles the in situ observations of vertical mixing better than the stronger mixing based on the standard configuration. This shows that the new calibration indeed improves the performance of the turbulence model.

1. Introduction

Since the late 1970s, satellite ocean color data have provided global time series of ocean surface chlorophyll-*a* (Chl *a*) concentration. Surface Chl *a* tracks most of the annual growth cycle of phytoplankton, including rapid changes in surface Chl *a* at the end of winter, known as spring blooms. While details of the mechanism leading to a spring bloom are still under debate (Behrenfeld and Boss 2014), upper-ocean vertical mixing and stratification are commonly recognized as the main drivers of the bloom. Numerous model studies using phytoplankton models have investigated the (combined and individual) effects of vertical mixing, nutrient supply and light limitation on the phytoplankton growth with idealized vertical mixing (Huisman et al. 1999; Klausmeier and Litchman 2001; Huisman and Sommeijer 2002; Ryabov et al. 2010; Mellard et al. 2011), modeled vertical mixing based on meteorological forcing (Allen et al. 2004; Johnk et al. 2008) and measured vertical mixing (Hahn-Woernle et al. 2014). All these studies indicate that phytoplankton growth depends strongly on the characteristics of the applied vertical mixing profile. Moreover, the simulated surface concentration of phytoplankton cells exhibits a strong correlation to the strength and shape of the vertical mixing (Hahn-Woernle et al. 2014).

Over the last few decades, an increasing number of observations of the upper-ocean turbulent properties have become available [see, e.g., Waterhouse et al. (2014) for an overview]. In situ observations provide an essential insight into the physical state of the upper ocean, but they remain scarce because obtaining them is time and cost intensive. Hence, numerical turbulence models cannot only bridge gaps in the observations but are also an essential tool to study turbulent mixing over

Corresponding author address: Lisa Hahn-Woernle, Institute for Marine and Atmospheric Research Utrecht (IMAU), Dept. of Physics and Astronomy, Utrecht University, P.O. Box 80005, 3508 TA Utrecht, Netherlands.
E-mail: l.hahn-woernle@uu.nl

DOI: 10.1175/JTECH-D-16-0053.1

long temporal and wide spatial scales. Turbulence models of different complexity in their closure schemes are used to derive turbulent characteristics of the upper ocean using meteorological observations. The General Ocean Turbulence Model (GOTM) provides a collection of such models that all use air–sea fluxes of momentum, heat and moisture, and subsurface profiles of shear and buoyancy frequency to predict profiles of turbulent properties (Umlauf and Burchard 2005). A common choice to simulate turbulent flows is the k–ε model, which solves transport equations of the turbulent kinetic energy k ($m^2\,s^{-1}$) and of the turbulent dissipation rate ε ($m^2\,s^{-3}$). Like other turbulence models, the k–ε model relies on the empirical parameterization of physical processes that are usually calibrated using laboratory or field data (Schumann and Gerz 1995; Canuto et al. 2001).

The sensitivity of model results to the value of the empirical parameters requires reliable calibration techniques (Olbert et al. 2014). Data assimilation methods have proven very efficient for the parameter calibration of turbulence models based on observations. Yu and Obrien (1991) assimilated observations of the Long-Term Upper Ocean Study-3 (LOTUS-3) buoys (by WHOI) to estimate the wind stress drag coefficient and profiles of the oceanic vertical eddy viscosity profile. Zhang et al. (2015) assimilated temperature profiles to determine wave-affected parameters using a second-order closure turbulence model. Both studies make use of a variational assimilation technique and vertical in situ observations of the upper ocean. The identical twin experiment (or identical synthetic experiment framework) of Zhang et al. (2015) shows that temperature observations at different depths are necessary to efficiently constrain the model results. However, time series of vertical upper-ocean observations are scarce and it is therefore timely to develop a methodology to calibrate parameters of a turbulence model based on ocean surface observations only. The benefit of such a method would be that the usage of satellite data would allow access to observations of a great spatial and temporal coverage. In this paper, we explore whether the coupling between vertical mixing and surface phytoplankton concentration is strong enough to estimate turbulence model parameters from observations of ocean surface Chl *a*.

As a model framework, we use the one-dimensional nutrient–phytoplankton (NP) model described in Hahn-Woernle et al. (2014) coupled to the k–ε model in GOTM. Biological parameters in the NP model have been calibrated using in situ data (including profiles of vertical mixing) from stations in the North Atlantic (Hahn-Woernle et al. 2014). The new element here is that surface Chl *a* data are used to calibrate model parameters in GOTM. The resulting profiles of the vertical mixing are then evaluated against the observed ones. Both identical twin experiments and the application to MODIS *Aqua* Chl *a* data show the capabilities and sensitivities of the methodology. The paper is concluded with a summary and a discussion of the applicability of the novel calibration method.

2. Methods and material

a. Observations and data

During summer 2009 (15 July–9 August) and spring 2011 (6 April–3 May), members of the STRATIPHYT project (ST) measured the biological, chemical, and physical properties of the upper ocean (<200-m depth) along a transect in the northeast Atlantic Ocean from Las Palmas de Gran Canaria (27°55′N, 15°22′W) to Reykjavik, Iceland (64°6′N, 21°50′W) on board the R/V *Pelagia* (Fig. 1; Mojica et al. 2015). Along the transect the ship stopped at 32 stations to take water samples and CTD measurements (standard conductivity, temperature, and pressure sensors) and to measure chlorophyll autofluorescence, light transmission, and photosynthetic active radiation (PAR).

High-resolution profiles of temperature and conductivity were taken over the upper 100 m with a Self-Contained Autonomous Microprofiler (SCAMP) at 15 (18) of the 32 stations during summer (spring). Jurado et al. (2012a,b) derived the vertical mixing coefficient K_T from the temperature variance dissipation rate χ_T according to (Osborn and Cox 1972)

$$K_T = \frac{\chi_T}{2}\left(\frac{\partial \overline{T}}{\partial z}\right)^{-2} \quad \text{with} \quad \chi_T = 6\nu^T\overline{\left(\frac{\partial T'}{\partial z}\right)^2}, \qquad (1)$$

where T describes the vertical temperature profile and ν^T is the molecular diffusivity of heat ($\approx 1.4\times10^{-7}\,m^2\,s^{-1}$). The overbar indicates a trimmed, smoothed, sharpened, filtered, and depth-binned quantity and T' is the temperature fluctuation part. A detailed description is given by Jurado et al. (2012b). Figures 1b and 1c show that stations south of 48°N were stratified during spring and summer, while stations north of 48°N were homogeneously mixed over the upper 100 m in spring and stably stratified with mixed layer depths (MLDs) between 20 and 45 m in summer. Following Levitus et al. (2000), the MLD is defined as the depth at which the temperature difference with the surface temperature just exceeds 0.5°C. Values of K_T varied between 10^{-6} and $10^{-1}\,m^2\,s^{-1}$ in summer and between 10^{-5} and $1\,m^2\,s^{-1}$ in spring.

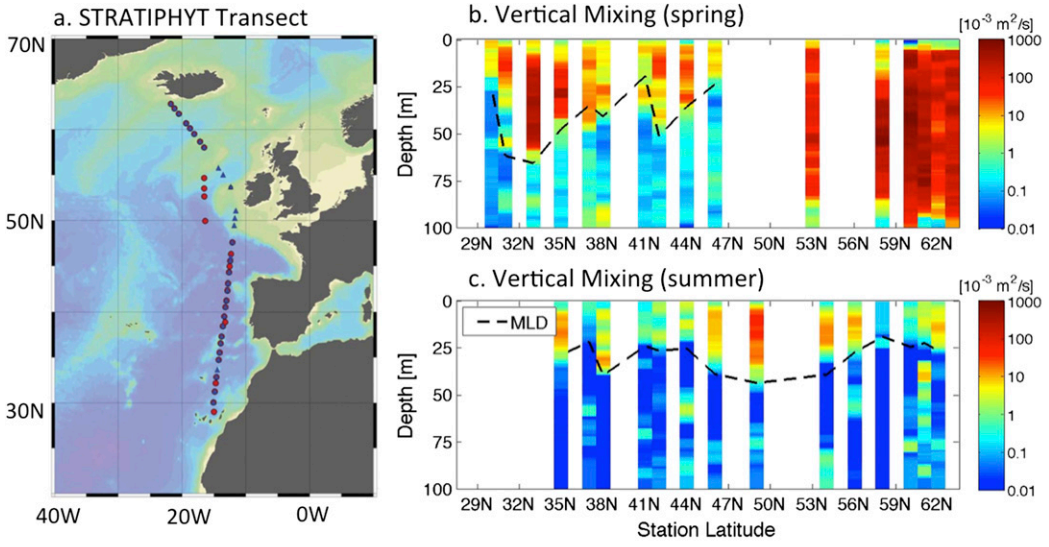

FIG. 1. (a) Ocean Data View (ODV) (Schlitzer 2002) bathymetric map of the northeast Atlantic Ocean depicting station locations for the fall 2009 (blue triangles) and spring 2011 (red circles) STRATIPHYT cruises (Mojica et al. 2015). Vertical mixing measured along the transect given in (a) during (b) spring 2011 and (c) summer 2009 (Jurado et al. 2012b,a).

Jurado et al. (2012a,b) found that within the mixed layer, the strength of the observed vertical mixing correlated with the wind speed for the stratified stations but not for the homogeneously mixed stations in spring. This indicates that the strong spring mixing has to be attributed to convective events that prevent the restratification above the maximum depth of the observations. For most stratified stations, the mechanically (wind) generated turbulence was suppressed by the stable stratification. Part of the uncertainty about the drivers of the vertical mixing originates from the fact that microstructure profiles were measured around noon. Nighttime convective mixing is therefore not captured while it contributes to the measured state.

Based on the water samples, Mojica et al. (2015) analyzed the phytoplankton community structure. Results show that stratification has a strong impact on the growth and distribution of different phytoplankton functional types. For stratified stations two dominant types were determined: picocyanobacteria and picoeukaryotic phytoplankton. Picocyanobacteria are associated with higher temperatures and high water clarity (deep euphotic zone) and were dominant in the southern part of the transect, while picoeukaryotic phytoplankton are associated with a higher nutrient flux in surface layers and are found in the northern part of the transect. The euphotic zone defines the part of the upper ocean in which irradiance is stronger than 0.1% of the surface value (Moore and Chisholm 1999). Also based on the water samples, van de Poll et al. (2013) determined the concentrations of inorganic PO_4, NO_2, and NO_x, which are here generalized to one nutrient concentration. Measurements show a northward increase in nutrient availability along the transect, and the mixed layer is generally depleted of nutrients at stations south of 48°N (40°N) in summer (spring).

MODIS *Aqua* surface Chl *a* data provide information about the phytoplankton growth over a longer period [standard Chl *a* level 3 products based on the full-mission ocean color reprocessing (R2014.0) by the Ocean Biology Processing Group]. Figure 2 shows 8-day mean Chl *a* concentrations for the years 2009 and 2011 averaged over a 1° × 1° box centered around ST station

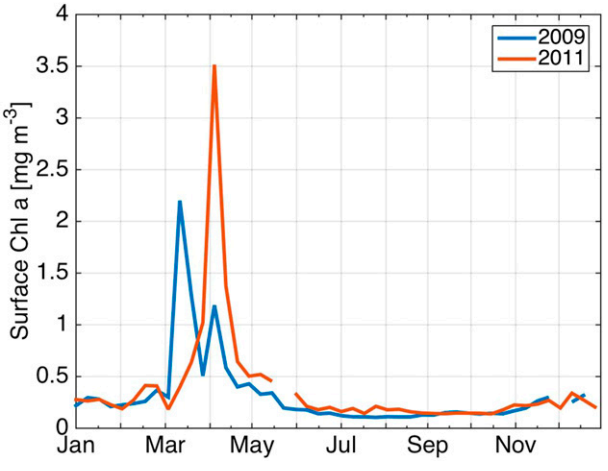

FIG. 2. MODIS *Aqua* surface Chl *a* 8-day mean for 2009 and 2011. Data are averaged over a 1° × 1° box centered around the STRATIPHYT station 11 in the North Atlantic (40.5°N, 13.2°W). Gaps are caused by persistent cloud cover.

TABLE 1. Variables used in GOTM (Burchard and Bolding 2001).

Symbol	Description	Units
	Mean flow variables	
(U, V)	Horizontal velocity field	$m\,s^{-1}$
Θ	Potential temperature	°C
S	Salinity	psu
P_R	Reference pressure	Pa
B	Buoyancy	$m\,s^{-2}$
$\langle\rho\rangle$	Potential density	$kg\,m^{-3}$
	k–ε model	
k	Turbulent kinetic energy	$m^2\,s^{-2}$
ε	Dissipation rate of k	$m^2\,s^{-3}$
ν_t	Turbulent diffusivity of momentum	$m^2\,s^{-1}$
ν_t^B	Turbulent diffusivity of heat (vertical mixing)	$m^2\,s^{-1}$
ν_{tm}, ν_{tm}^B	Minimum background diffusivity	$m^2\,s^{-1}$
ν	Molecular diffusivity of momentum	$m^2\,s^{-1}$
ν^Y	Molecular diffusivity of mean flow variable Y	$m^2\,s^{-1}$
P_S	Shear production	$m^2\,s^{-3}$
G	Buoyancy production	$m^2\,s^{-3}$
M	Background shear frequency	s^{-1}
N_b	Buoyancy frequency	s^{-1}
$c_{\varepsilon 1,..,3}$	Production term parameters (Rodi 1987)	

11 at 40.5°N, 13.2°W. In 2009, the bloom (increased surface Chl *a*) started in early March and peaked around 14 March 2009. The surface concentration increased roughly by a factor of 5 and decreased quickly after the peak. In 2011, the bloom was initiated also in early March, but it developed slower peaking in early April. Apart from occurring almost a month later than in 2009, surface Chl *a* increased roughly by a factor of 7, leading to an intense and sharp bloom. In both years, surface Chl *a* remains low from May onward.

The atmospheric forcing for GOTM is based on ERA-Interim for the years 2005–11 provided by ECMWF (downloaded 30 March 2015; Dee et al. 2011). Data are selected at midnight and noon for the wind vector at 10-m height, the surface pressure, the air temperature at 2-m height, the dewpoint temperature at 2-m height, and the medium cloud cover. In GOTM, these atmospheric forcing data in combination with the coordinates and the date are used to derive the shortwave radiation and atmospheric fluxes, such as the heat flux and the momentum flux.

b. Model component: GOTM

GOTM is a collection of one-dimensional physical models to describe the interaction between thermodynamic and hydrodynamic processes related to vertical mixing in the water column (Burchard and Petersen 1999). Here, the k–ε model is used with a similar setup as in Allen et al. (2004). Below, the basic equations are briefly outlined. A detailed description is given in Burchard and Bolding (2001) and therein cited literature; in Table 1 all variables are defined.

BASIC EQUATIONS OF THE $K-\varepsilon$ MODEL

On a vertical domain $z \in [0, Z_b]$, where $z = 0$ indicates the surface and $z = Z_b$ (300 m) indicates the bottom boundary, the transport equations for k and ε are given by

$$\frac{Dk}{Dt} = \frac{\partial}{\partial z}\left(\frac{\nu_t}{\sigma_k}\frac{\partial k}{\partial z}\right) + P_S + G - \varepsilon \tag{2}$$

and

$$\frac{D\varepsilon}{Dt} = \frac{\partial}{\partial z}\left(\frac{\nu_t}{\sigma_\varepsilon}\frac{\partial \varepsilon}{\partial z}\right) + \frac{\varepsilon}{k}(c_{\varepsilon 1}P_S + c_{\varepsilon 3}G - c_{\varepsilon 2}\varepsilon)\,, \tag{3}$$

respectively, where D/Dt denotes the material derivative $\partial/\partial t + W\partial/\partial z$ with the mean vertical advection W, and σ_k and σ_ε are the constant Schmidt numbers for k and ε, respectively. At 100-m depth, W is prescribed to $1 \times 10^{-9}\,m\,s^{-1}$ and decreases linearly to zero toward the upper and lower boundaries. The water column is assumed to be horizontally homogenous over the area of interest and horizontal advection is neglected.

The shear production P_S is given by

$$P_S = \nu_t M^2 \quad \text{where} \quad M = \sqrt{\left(\frac{\partial U}{\partial z}\right)^2 + \left(\frac{\partial V}{\partial z}\right)^2}\,, \tag{4}$$

where M is the background shear frequency in terms of the mean horizontal velocity field (U, V). The buoyancy production G is given by

$$G = -\nu_t^B N_b^2 \quad \text{with} \quad N_b = \sqrt{-\frac{g}{\rho_0}\frac{\partial\langle\rho\rangle}{\partial z}}, \tag{5}$$

where N_b is the buoyancy frequency, g is the gravitational acceleration, and ρ_0 is the reference density. The mean potential density $\langle\rho\rangle$ is calculated with the United Nations Educational, Scientific and Cultural Organization (UNESCO) equation of state and the mean flow variables salinity S and potential temperature Θ, as well as the mean reference pressure P_R (Fofonoff and Millard 1983). A detailed description of the production terms and the atmospheric fluxes is given in appendix A.

Turbulent mixing distributes a mean flow variable Y (see definition in appendix A) as a part of the sum of turbulent and viscous transport terms:

$$\mathscr{D}_Y = \frac{\partial}{\partial z}\left[(\nu_* + \nu^Y)\frac{\partial Y}{\partial z}\right]. \tag{6}$$

In the case of $Y = U$ and $Y = V$, $\nu_* = \nu_t$ is the turbulent diffusivity of momentum. In the case of mean Θ and mean S, $\nu_* = \nu_t^B$ is the turbulent diffusivity of heat. The model variable ν_t^B and the measured K_T quantify

vertical mixing caused by turbulent processes. The two different assignments help to distinguish between model and observations, and allow conformity with existing notations by Burchard and Petersen (1999) and Jurado et al. (2012a,b). Note that ν_t^B is also applied to biological model variables. The molecular diffusivity of Y is given by ν^Y.

The turbulent diffusivity of momentum ν_t and the turbulent diffusivity of heat ν_t^B are calculated with a downgradient approximation:

$$\nu_t = c_\nu \frac{k^2}{\varepsilon} + \nu_{tm} \quad \text{and} \quad \nu_t^B = c'_\nu \frac{k^2}{\varepsilon} + \nu_{tm}^B, \tag{7}$$

where c_ν and c'_ν are stability functions (Schumann and Gerz 1995). Here, the minimum background mixing terms ν_{tm} and ν_{tm}^B are added to the standard k–ε model. They are both set to $10^{-5}\,\mathrm{m\,s^{-2}}$ and guarantee a minimum supply of nutrients from the lower boundary to the euphotic zone. The MLD is derived from the profile of ν_t^B and is defined as the minimum depth for which $\nu_t^B \le 10^{-4}\,\mathrm{m\,s^{-2}}$ holds [based on Umlauf and Burchard (2005), adapted to ν_{tm}^B]. According to this definition, the mixed layer tracks variations of the vertical mixing instantaneously and is not comparable to temperature-based definitions of the MLD (e.g., Levitus et al. 2000).

The parameters $c_{\varepsilon i}$, $i = 1, \ldots, 3$ in Eq. (3) control the relative importance of P_S and G to ε. The values $c_{\varepsilon 1} = 1.44$ and $c_{\varepsilon 2} = 1.92$ are empirically determined and constant. The value of $c_{\varepsilon 3}$ is different for stably stratified states ($G \le 0$) and unstably stratified states ($G > 0$):

$$c_{\varepsilon 3} = \begin{cases} c_{\varepsilon 2} - \dfrac{c_\mu}{c_{\mu'}} \dfrac{c_{\varepsilon 2} - c_{\varepsilon 1}}{\mathrm{Ri}_{\mathrm{st}}} & \text{for} \quad G \le 0 \\ c_{\varepsilon 3+} & \text{for} \quad G > 0. \end{cases}$$

The general Richardson number $\mathrm{Ri} = N_b^2/M^2$ expresses the ratio of buoyancy frequency to shear frequency. The steady-state Richardson number $\mathrm{Ri}_{\mathrm{st}}$ (standard value of 0.25) refers to the value of Ri for a homogeneous stratified shear flow in steady state.

In the standard configuration, the value $c_{\varepsilon 3+} = 1$ is based on Rodi (1987), but the value has been under debate (Baumert and Peters 2000). This and its direct impact on the convection-driven winter mixing ($G > 0$) motivated us to choose $c_{\varepsilon 3+}$ as a calibration parameter. Increasing $c_{\varepsilon 3+}$ in the unstable state increases ε. It follows for large $c_{\varepsilon 3+}$ that more kinetic energy is lost to heat and less remains for mixing. This reduces the unstably stratified part of the water column and thereby the strength of the winter mixing. The reverse is the case if $c_{\varepsilon 3+}$ is decreased.

c. Model component: NP

The NP model is based on the advection–reaction–diffusion models by Huisman and Sommeijer (2002) and Ryabov et al. (2010). At time $t > 0$ and vertical position $z \in [0, Z_b]$, the one-dimensional water column of depth Z_b contains nutrients $N(z, t)$ and phytoplankton $P(z, t)$. The column is forced by a depth- and time-dependent vertical mixing $\nu_t^B(z, t)$ computed with GOTM. Phytoplankton growth depends on $N(z, t)$ and the intensity of available PAR $I_{\mathrm{PAR}}(z, t)$ (Huisman and Sommeijer 2002; Ryabov et al. 2010) according to

$$\begin{aligned} \frac{\partial P}{\partial t} &= \text{growth} - \text{loss} - \text{sinking} + \text{mixing} \\ &= \mu(N, I_{\mathrm{PAR}})P - mP - \nu \frac{\partial P}{\partial z} + \frac{\partial}{\partial z}\left[\nu_t^B(z,t)\frac{\partial P}{\partial z}\right], \end{aligned} \tag{8}$$

where $\mu(N, I_{\mathrm{PAR}})$ describes the local growth rate, m is the mortality, and ν is the sinking velocity. Uptake and recycling couple nutrients and phytoplankton:

$$\begin{aligned} \frac{\partial N}{\partial t} &= -\text{uptake} + \text{recycling} + \text{mixing} \\ &= -\alpha\mu(N, I_{\mathrm{PAR}})P + \varepsilon\alpha m P + \frac{\partial}{\partial z}\left[\nu_t^B(z,t)\frac{\partial N}{\partial z}\right], \end{aligned} \tag{9}$$

where α is the nutrient content of a phytoplankton cell and ε is the nutrient recycling coefficient. Horizontal gradients of the growth-controlling factors (nutrient and PAR availability) are assumed to be negligible in comparison to vertical gradients over the area of interest ($1° \times 1°$ box centered around the ST station).

The growth rate $\mu(N, I_{\mathrm{PAR}})$ depends on the local availability of light and nutrients:

$$\mu(N, I_{\mathrm{PAR}}) = \mu_{\max} \min\left(\frac{N}{H_N + N}, \frac{I_{\mathrm{PAR}}}{H_I + I_{\mathrm{PAR}}}\right), \tag{10}$$

where $\mu_{\max}$ is the maximum growth rate of phytoplankton and H_N and H_I are the half-saturation constants of nutrients and light, respectively. The half-saturation constants are used to determine the relative dependence of the phytoplankton growth on the two resources. For example, H_N is relatively high for species whose growth is controlled by nutrient limitation.

The intensity of $I_{\mathrm{PAR}}(z, t)$ decreases with depth due to the constant background turbidity K_{bg} and the shading by phytoplankton cells represented by the absorption coefficient K:

$$I_{\mathrm{PAR}}(z) = \min(I_{\mathrm{in}}, I_{\min}) \exp\left[-K_{\mathrm{bg}} z - K \int_0^z P(\xi, t)\, d\xi\right], \tag{11}$$

TABLE 2. Parameters and variables used in the GOTM-NP for the location 40.5°N, 13.2°W.

Symbol	Description	Units	Value
	System parameters		
Z_b	Depth of system	m	300
Z_N	Depth of nutrient reservoir	m	200[a]
N_{Zb}	Nutrient concentration at Z_N based on ST observations	mmol nutrients m^{-3}	5.30
	Optical parameters		
K_{bg}	Background turbidity	m^{-1}	0.032
K	Absorption coefficient of phytoplankton	m^2 $cell^{-1}$	1.0×10^{-9}
I_{min}	Minimum I_{in} (for NP only)	W m^{-2}	20[a]
β	Conversion factor shortwave radiation ($\lambda = 550$ nm)	(μmol photons m^{-2} s^{-1}) (W m^{-2})$^{-1}$	$\lambda \cdot 8.36 \times 10^{-3}$
	Biological parameters		
μ_{max}	Maximum specific growth rate	h^{-1}	0.08[a]
H_I	Half-saturation constant of light-limited growth	W m^{-2}	18.486
H_N	Half-saturation constant of nutrient-limited growth	mmol nutrients m^{-3}	0.1001[b]
m	Specific loss rate	h^{-1}	0.01
α	Nutrient content per phytoplankton cell	mmol nutrient $cell^{-1}$	1.0×10^{-9}
γ	Chl *a* content per phytoplankton cell	(mg Chl *a*) $cell^{-1}$	5.0×10^{-9}
ε	Nutrient recycling coefficient	—	0.6170[b]
ν	Sinking velocity	m h^{-1}	0.0025
	Variables		
$P(z, t)$	Phytoplankton concentration	cells m^{-3}	
$N(z, t)$	Nutrient concentration	mmol nutrients m^{-3}	
$I_{PAR}(z, t)$	Intensity of photosynthetic active radiation	W m^{-2}	

[a] Parameter adapted after the migration from the NP model used for the calibration (constant forcing) to GOTM-NP (forced by seasonal and daily cycles). See appendix B for details.
[b] Calibrated values representing nutrient-limited growth (Hahn-Woernle et al. 2014).

where I_{in} is the photosynthetic active part of the incoming shortwave radiation with I_{min} guaranteeing a minimum light availability (see appendix B).

Neumann boundary conditions are defined for P at the upper and lower boundaries:

$$\left[\nu P - \nu_t^B(z,t)\frac{\partial P}{\partial z}\right]\Bigg|_{z=0,Z_b} = 0. \tag{12}$$

The same holds for N at the upper boundary, while at depth $Z_N = 200$ m N is kept constant, representing the nutrient reservoir of the deep ocean:

$$\left.\frac{\partial N}{\partial z}\right|_{z=0} = 0 \quad \text{and} \quad N(Z_N) = N_{Zb}. \tag{13}$$

Hahn-Woernle et al. (2014) calibrated biological and optical parameters of the NP model to in situ (ST) measurements of Chl *a* and nutrients under stably stratified conditions in summer. The calibrated parameters used in this study represent a picocyanobacteria-dominated situation that has an early and short bloom in spring and grows under nutrient-limited conditions below the mixed layer in summer. Standard and calibrated parameters are listed in Table 2.

The NP model is embedded in the GOTM following the setup of the nutrient–phytoplankton–zooplankton–detritus (NPZD) model of the Framework for Aquatic Biogeochemical Models (FABM) toolbox (http://www.fabm.net). Diffusion is solved fully implicit, vertical advection is solved first-order upwind and fully monotone, and a forward Euler method is used to solve the ordinary differential equations. The time step used for the forward Euler method is one-tenth of the GOTM time step to guarantee a stable model performance.

d. Model initialization

GOTM-NP is run in two ways: first, a long equilibrium run is done; then, GOTM-NP is restarted from an equilibrium state. The equilibrium run is initialized with ST observations of S, Θ, ε, P, and N (the initial velocity field is zero). Then the model is run for 20 years with repeated atmospheric forcing of the years 2005–09, which guarantees that the mean flow variables and the biological variables are in equilibrium with the forcing. For a restart, GOTM-NP is initialized with profiles of S, Θ, ε, U, V, P, and N of the equilibrium run corresponding to the day of the restart. For example, below GOTM-NP is run for the years 2008 and 2009. The initialization for this simulation is based on 1 January 2008 after 18 years of the equilibrium run.

e. Model component: OpenDA

For the calibration of one of the parameters in GOTM—say, λ—based on observations of surface Chl *a*, we use the

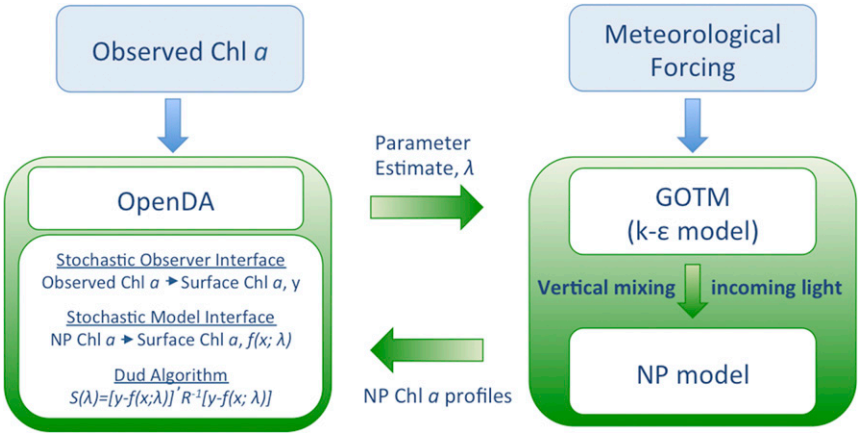

FIG. 3. Schematic setup of the OpenDA–GOTM-NP coupling. Blue elements are identical for all calibration iterations, while green elements are updated at each iteration. Note that the vertical mixing and the incoming PAR intensity are passed to the NP model on every GOTM time step. NP Chl *a* profiles are passed to OpenDA after the GOTM simulation is finished.

calibration and data assimilation toolbox OpenDA (http://www.openda.org). This toolbox offers a modular framework for parameter calibration and data assimilation that is coupled to the model of interest via a stochastic model interface and to the observations via a stochastic observer interface. For the calibration, the Doesn't Use Derivative (DUD) algorithm is used (Ralston and Jennrich 1978). Even though this algorithm is part of an assimilation toolbox, it only calibrates a model parameter to observations by minimizing a cost function.

Suppose there is one uncertain model parameter $\lambda \in \Re$ and a set of n observations $y \in \Re^n$ is available. The parameter λ is then calibrated by minimizing the following cost function:

$$S(\lambda) = [y - f(x;\lambda)]' \mathbf{R}^{-1} [y - f(x;\lambda)], \qquad (14)$$

where $f: \Re^d \rightarrow \Re^n$ projects the model state $x \in \Re^d$ (depending on λ) on the observations. The diagonal covariance matrix $\mathbf{R}$ is determined by the square of the observational noise σ. The best fit is defined as the value of λ with the minimum cost function $S(\lambda)$. In appendix C the calibration procedure is described.

f. Implementation

In Fig. 3 an overview of the model components is given. In this work, the calibration parameter is $c_{\varepsilon 3+}$, but for simplicity the general variable λ is used in the following description of the calibration method.

A typical calibration loop starts by passing λ (initial guess or DUD estimate) via a namelist file to GOTM and a new GOTM-NP run is performed. GOTM is forced by ECMWF meteorological data and calculates among other quantities the vertical mixing and incoming light intensity with which the NP model is forced. After the run is completed (e.g., from 2008 to 2009), the GOTM-NP model output is passed to OpenDA. The model state x is defined by the vertical Chl *a* profiles and with $f(x;\lambda)$ the modeled surface Chl *a* is determined as mean over the uppermost 15 m of the Chl *a* profile. Since the GOTM forcing for the NP model depends on the choice of λ, the modeled surface Chl *a* becomes also a function of λ. With the DUD algorithm, $S(\lambda)$ is calculated from the satellite observations and the model output [Eq. (14)]. If needed, a new parameter estimate λ^* is determined. New calibration iterations are initiated until one of the stopping criteria is reached [e.g., cost tolerance is achieved, $S(\lambda) \leq S_{\text{tol}}$].

3. Results

Figure 4 shows GOTM-NP results derived from the standard calibration of the k–ε model parameters forced with meteorological data of 2009. Winter mixing is strong and reaches to over 200-m depth until mid-March (Fig. 4d). The strong mixing transports nutrients into the euphotic zone, allowing for a long and intense bloom after the mixing weakens in early April, a so-called upper chlorophyll maximum (UCM; Fig. 4b). By July all nutrients are depleted in the mixed layer (Fig. 4c) and a deep chlorophyll maximum (DCM) establishes just below the mixed layer. Ongoing nutrient limitation forces the DCM deeper and deeper. Only as the MLD reaches below 43-m depth in November, Chl *a* and nutrients are diluted in the mixed layer and a UCM is established again.

In situ data of mid-April 2011 show that the mixed layer is nutrient limited and most phytoplankton are found in a DCM (Mojica et al. 2015). Comparing the surface Chl *a* signals of 2009 and 2011 in Fig. 2, it is

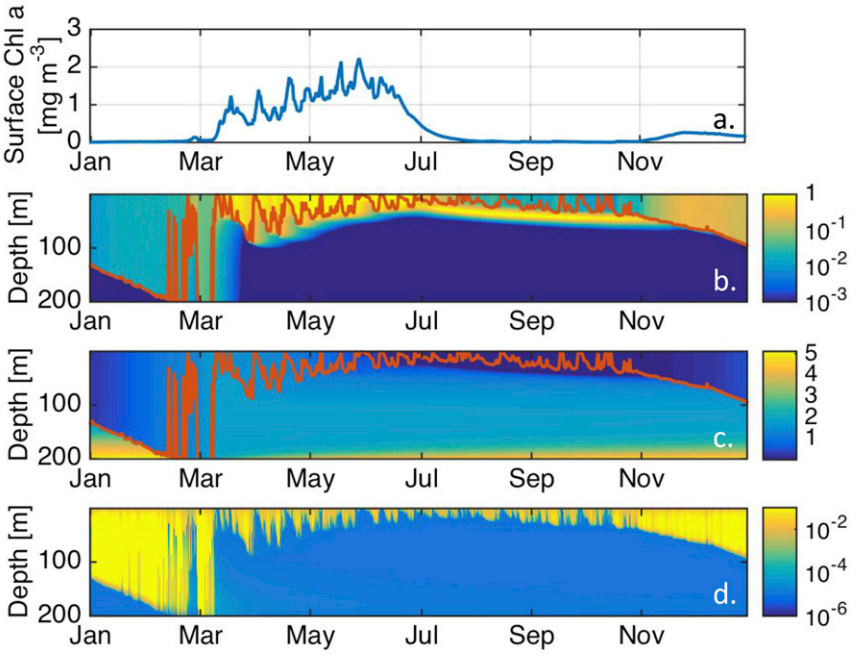

FIG. 4. True model results for the ITE with $c_{\varepsilon 3+} = 1.0$ based on meteorological forcing of 2009. (a) Surface Chl *a* (mean over 0–15 m), (b) Chl *a* (mg m^{-3}), (c) nutrients (mmol m^{-3}), and (d) vertical mixing (m^2 s^{-1}). Red line indicates the MLD (minimum depth with $\nu_t^B \leq 1e^{-4}$).

reasonable to assume that the upper ocean in spring 2009 was in a similar nutrient-limited state. It follows that the modeled winter mixing and the resulting nutrient supply are too strong in the standard version of GOTM. Analysis of the model results for the winter mixing in 2009 showed that mixing is not only wind but also convection driven. Since $c_{\varepsilon 3+}$ has an effect only on the unstable case, it is a very effective parameter to improve the modeled winter mixing and is therefore chosen for the calibration. The calibration method is tested in two ways: first, with the help of identical twin experiments (ITEs) to gain knowledge about the capabilities and sensitivities of the method (section 3a); and second, with the use of MODIS *Aqua* satellite data of surface Chl *a* (section 3b). In all cases, the GOTM-NP model is run for two years with the first year being the spinup and data of the second year are used for the analysis and calibration.

a. Identical twin experiment

The *true* scenario for the ITEs is based on the surface Chl *a* signal of 2009 (Fig. 4a) modeled with $c_{\varepsilon 3+} = 1.0$ (standard value in the GOTM setup).

1) EFFECT OF $c_{\varepsilon 3+}$ ON THE VERTICAL MIXING

Since $c_{\varepsilon 3+}$ is a relatively abstract parameter, the sensitivity of the vertical mixing to changes of $c_{\varepsilon 3+}$ and its consequences for the Chl *a* abundance are presented prior to the ITE results. As discussed in section 2b, increasing $c_{\varepsilon 3+}$ leads to an increase of ε in the unstable state and thereby to more energy being dissipated to heat. In Fig. 5, the correlation of vertically averaged [50–100 m] values of ν_t^B and ε are plotted for 12-hourly data from 1 January to 31 March 2009. Results show that as

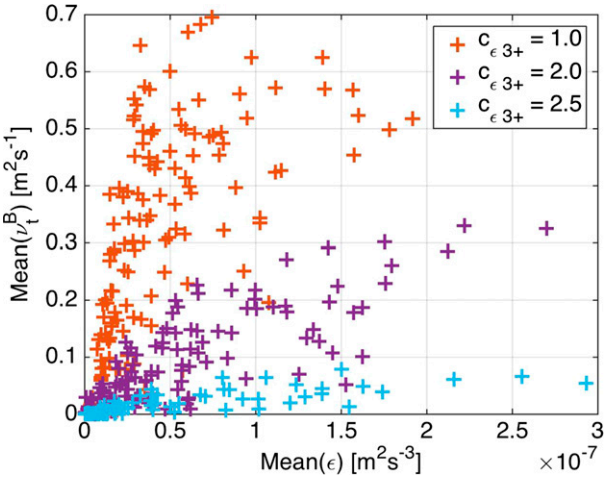

FIG. 5. Relation of ν_t^B to ε for different values of $c_{\varepsilon 3+}$. Data points represent the vertical mean over 50–100 m of ν_t^B and ε for 12-hourly data between 1 Jan and 31 Mar 2009. Turbulent properties are most dominantly affected by $c_{\varepsilon 3+}$ over this depth interval and during this period.

more energy dissipates into heat, the less energy that is available for vertical mixing, which leads to a more stratified water column.

In Fig. 6 the effect of $c_{\varepsilon 3+}$ on the depth of the mixed layer, surface Chl *a*, and surface nutrients is shown for the year 2009. Winter mixing weakens with increasing $c_{\varepsilon 3+}$, even drastically for values higher than 2.0 (Fig. 6a). Between March and May, the surface Chl *a* signal is almost identical for cases with deep winter mixing (Fig. 6b). By June, the concentrations start to differ, caused by the differences in winter mixing. For $c_{\varepsilon 3+} = 0.5$, the maximum MLD is 223 m, which leads to a bloom that lasts for four months and has a maximum surface Chl *a* of 2.5 mg m^{-3}. For $c_{\varepsilon 3+} = 2.0$, the maximum MLD is 195 m, which leads to a bloom that lasts for only three months and has a maximum surface Chl *a* of 1.7 mg m^{-3}. The drastic change in winter mixing caused by $c_{\varepsilon 3+} = 2.5$ has also substantial consequences for the surface Chl *a* values: the bloom occurs in early January and it is short (one month) and weak (maximum surface Chl *a* of 0.26 mg m^{-3}). An explanation is found from the surface nutrient concentrations (Fig. 6c): deeper mixing leads to more nutrients in the surface layer, sustaining a longer and stronger bloom.

To show the relation between vertical mixing and nutrient supply more quantitatively, the nutrient flux ρ_N is calculated as (Hahn-Woernle et al. 2014)

$$\rho_N = -\left\langle \nu_t^B \frac{\partial N}{\partial z} \right\rangle_z, \tag{15}$$

where $\langle a \rangle_z$ gives the vertical average of the quantity *a* from the surface to the depth of the fixed nutrient boundary (200 m). Figure 7 shows that both the annual mean nutrient flux and the annual mean surface Chl *a* concentration decrease with increasing $c_{\varepsilon 3+}$. In other words, the decreasing vertical mixing provides less nutrients to the surface and thereby reduces the surface Chl *a*. For low values of $c_{\varepsilon 3+}$, the nutrient flux becomes less sensitive to changes, because only if mixing occurs over a gradient in the nutrient concentration, it contributes to the nutrient flux. A homogeneously mixed water column with homogeneous nutrient distributions therefore does not contribute to the nutrient flux. The surface Chl *a* still benefits from the nutrient supply at low values of $c_{\varepsilon 3+}$. However, eventually the light-limiting effect of too strong mixing leads to a halt or decrease in surface Chl *a* (not reached yet here).

The rapid transition to a strongly stratified water column for values of $c_{\varepsilon 3+} > 2.0$ limits the nutrient supply and surface Chl *a* decreases drastically. As soon as the stratification dominates the water column throughout the whole year, nutrients are not provided to the surface anymore and growth decays. A new equilibrium seems to be approached for $c_{\varepsilon 3+} \geq 2.5$, since the nutrient supply is hardly enough to allow growth and a further increase of $c_{\varepsilon 3+}$ will only intensify the stratification.

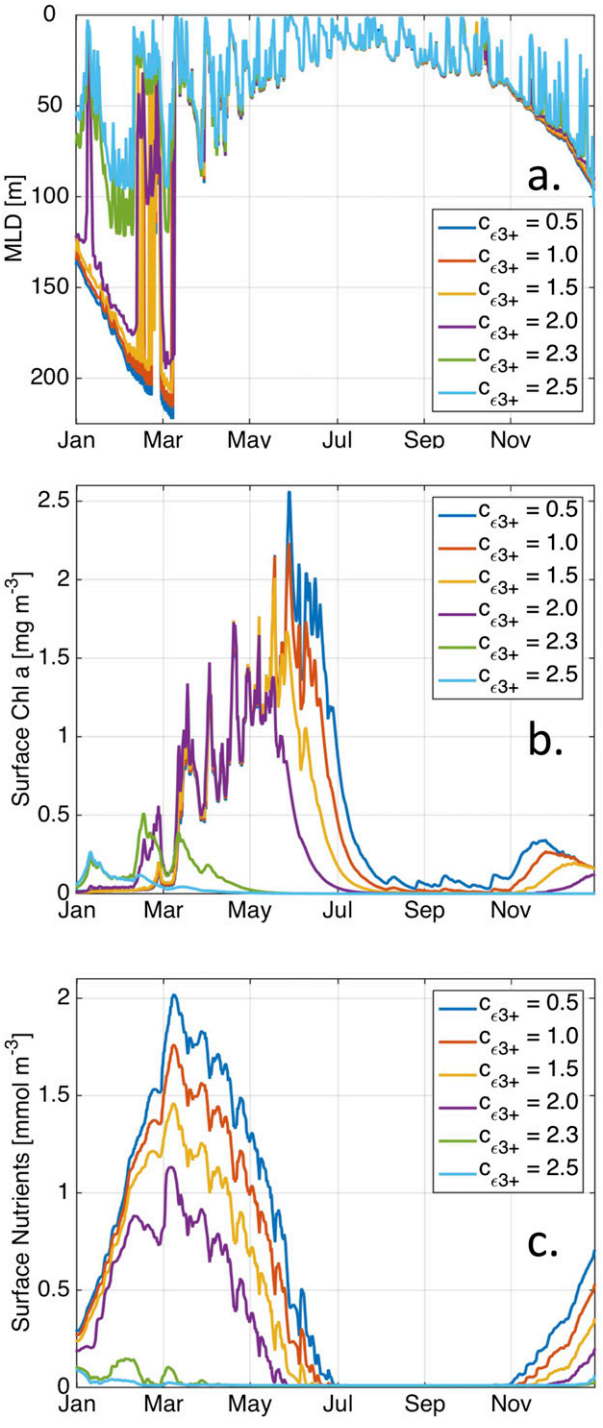

FIG. 6. Change in (a) MLD, (b) surface Chl *a*, and (c) surface nutrient concentration due to different values of $c_{\varepsilon 3+}$ for the forcing of 2009. Surface concentrations are calculated as the vertical mean over 0–15 m.

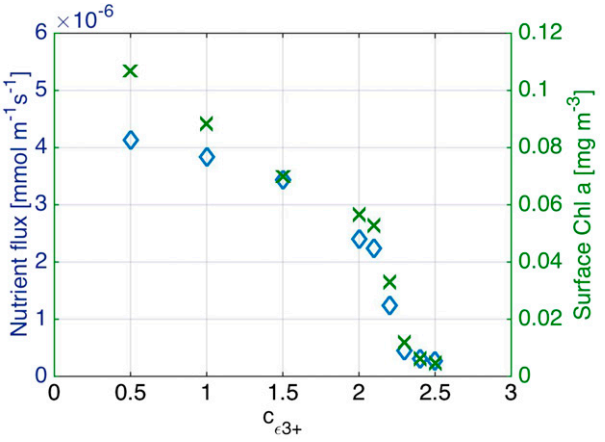

FIG. 7. Annual mean nutrient flux over 0 − 200 m, left axis, (blue diamonds) and annual mean surface Chl *a* over 0 − 15 m, right axis (green crosses) plotted as functions of $c_{\varepsilon 3+}$.

2) SENSITIVITY

Artificial observations for the ITEs are generated by adding noise to the surface Chl *a* curve shown in Fig. 4a. Each observation y_0 is perturbed by a value taken randomly out of a uniform distribution over the interval $[y_0 - \sigma, y_0 + \sigma]$. If the resulting value is negative, it is discarded.

In the standard setup of the calibration, 12-hourly artificial observations between January and the end of August (the main growth season) of the year 2009 are used to compute the cost function. If not stated otherwise, the standard noise amplitude is $\sigma = 0.05\,\text{mg Chl}\,a\,\text{m}^{-3}$ and GOTM-NP is initialized with $c_{\varepsilon 3+} = 2.0$ as the initial estimate. In the experiments below, we analyze the sensitivity of the method to the value of the noise amplitude, the sampling frequency, the sampling sequence, and the initial estimate of $c_{\varepsilon 3+}$. In Table 3, an overview of all experiments and their best fit (minimum *S*) for $c_{\varepsilon 3+}$ is given.

In a first series of experiments, the effect of observational noise on the performance of the calibration method is tested. Figure 8a shows an example of an artificial observation with $\sigma = 0.25\,\text{mg Chl}\,a\,\text{m}^{-3}$. The noise adds a higher variability to the data, but the main shape remains conserved. Calibrations with a noise between 0.005 and $0.5\,\text{mg Chl}\,a\,\text{m}^{-3}$ converge all to values of $c_{\varepsilon 3+} \in [0.926, 1]$ (1 being the true value) with decreasing accuracy as the noise increases (Table 3). A noise amplitude of $2.5\,\text{mg Chl}\,a\,\text{m}^{-3}$ is in the order of the surface concentration itself and the bad performance of the calibration method comes therefore as no surprise. Decreasing $c_{\varepsilon 3+}$ by ~8% of its initial value causes a 2.6% increase of total surface Chl *a* and a 3.3% increase of the maximum surface Chl *a* and of the total surface nutrients (cf. Fig. 6). The standard deviation of the difference between the two MLD time series is 0.5% of the mean MLD. These results show that the calibration yields to an accurate representation of the *truth* even with noisy observations.

TABLE 3. Overview of the initialization and the performance of the individual ITEs.

Experiment	Objective	$c_{\varepsilon 3+}$ estimate	RMSE
Noise (σ) (mg Chl a m^{-3})	0.005	0.9999	0.0029
	0.025	0.9988	0.0141
	0.05	0.9952	0.0278
	0.25	0.9872	0.1420
	0.5	0.9262	0.2880
	2.5	0.5	1.3816
Frequency	12 h	0.9952	0.0278
	24 h	1.0026	0.0282
	8 days	1.0214	0.0237
	16 days	1.0343	0.0291
	30 days	0.9789	0.0226
Sequence	Jan–Aug	0.9952	0.0278
	Jan–Jun	0.9958	0.0277
	Jan–Apr	0.9656	0.0273
	Feb–Mar	1.0089	0.0275
	Jul–Aug	0.9924	0.0283
Initial $c_{\varepsilon 3+}$	Feb	1.1476	0.0264
	Mar	0.9559	0.0282
	0.5	0.9953	0.0278
	1.5	0.9952	0.0278
	2.0	0.9952	0.0278
	2.5	0.9953	0.0278

The value of σ enters the calibration also via Eq. (14), since the diagonal elements of $\mathbf{R}$ are proportional to σ^2. This is shown in Fig. 8b: the smaller the σ, the higher the initial cost and vice versa (initial $c_{\varepsilon 3+}$ is identical for all cases). Since in the DUD algorithm only the minimum of *S* is important, the actual value of the cost is not relevant for the calibration of $c_{\varepsilon 3+}$. A more intuitive measure is the root-mean-square error (RMSE) of the artificial observations and the model simulations of surface Chl *a*. Values given in Table 3 show that the RMSE is mainly affected by the noise amplitude. As Fig. 8d shows, the true value for $c_{\varepsilon 3+}$ is generally approached within a few iterations, unless observations are too strongly affected by the noise (e.g., $\sigma = 2.5\,\text{mg Chl}\,a\,\text{m}^{-3}$).

The results above are based on observations sampled every 12 h. When working with real observations, sampling frequencies lie in the order of one observation per day or week, if not less frequent. Therefore, the effect of the sampling frequency of observations on the performance of the calibration method is analyzed. The chosen sampling intervals are 12 h, 1 day, 8 days, 16 days, and 30 days. After the sampling, a noise of

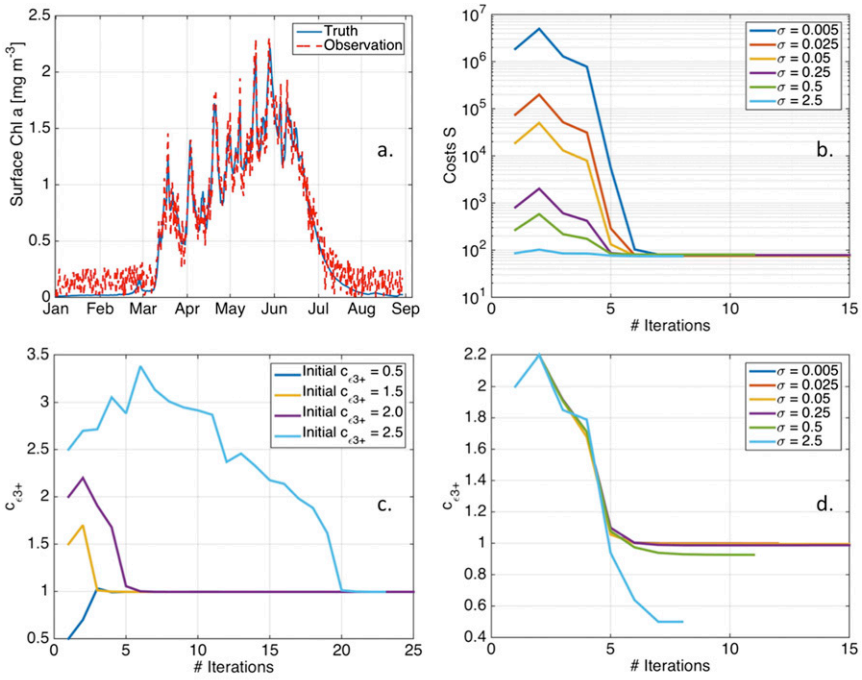

FIG. 8. Characteristics of the ITEs. (a) Artificial observations based on the true scenario ($c_{\varepsilon 3+}$ = 1.0, 2009 forcing) with randomly added noise, $\sigma \in [-0.25, 0.25]$ mg Chl a m^{-3}. (b) Evolution of S during the calibration for different values of σ. Logarithmic y-axis scale. The x axis counts the calibration iterations done to find a minimum of S. (c) Values of $c_{\varepsilon 3+}$ used during the calibration for different initializations of $c_{\varepsilon 3+}$. (d) Values of $c_{\varepsilon 3+}$ used during the calibration for different values of σ [same experiment as in (b)].

$\sigma = 0.05$ mg Chl a m^{-3} is applied to generate the artificial observations. Table 3 shows that the lower sampling frequencies lead to calibration results for $c_{\varepsilon 3+}$ that have a maximum deviation of 3% from the truth. Increasing $c_{\varepsilon 3+}$ by ~3% of its initial value causes a 2% decrease of total surface Chl a and a 3% decrease of the maximum surface Chl a and of the total surface nutrients. The standard deviation between the difference of the two MLD time series lies below 0.5% of the mean MLD. These results show that the calibration method has a high performance even at low sampling frequencies.

In the standard setup, the artificial observations are sampled between January and end of August. This period captures the main bloom and its main characteristics (e.g., timing). To test which and how much information about the bloom is needed, alternative periods are taken in this ITE. Results in Table 3 show that most of the calibrated parameters deviate by only 1% from the true value. One exception is the experiment with sampling only in February. Observed surface Chl a is in the range of the noise (0.25 mg Chl a m^{-3}) until the end of February, from which it follows that the observations provide little information, resulting in small variations of surface Chl a with changing $c_{\varepsilon 3+}$. Surprisingly even short sampling sequences, like the one based on March only, can lead to a good calibration result. This experiment shows that the sampling sequence should be well chosen and that it should contain at least one characteristic feature of the bloom to optimize the calibration result.

As shown in Fig. 6, the choice of $c_{\varepsilon 3+}$ has a strong effect on the different modeled properties. To test whether the performance of the calibration method is affected by the initial value of $c_{\varepsilon 3+}$, the method is initialized with $c_{\varepsilon 3+}$ = 0.5, 1.5, 2.0, and 2.5 (as in Fig. 6). In Fig. 8c all values of $c_{\varepsilon 3+}$ used during the calibration are plotted against the number of iterations. The farther the initial guess lies from the true value, the longer it takes to approach the best fit. Still, as Table 3 shows, the effect of the initial guess of $c_{\varepsilon 3+}$ on the final calibration is negligible.

b. *Calibration to satellite Chl* a

Having studied the capabilities of the calibration method in section 3a, the method is now applied to real observations of surface Chl a derived from satellite observations. In section 3b(1), GOTM-NP is forced with the same forcing as in the ITEs, but instead of artificial

TABLE 4. Overview of the calibration results based on satellite observations of the years 2009 and 2011 for the direct and normalized cases. RMSEs are also given for the standard value of $c_{\varepsilon 3+}$.

MODIS *Aqua* Surface Chl *a*	$c_{\varepsilon 3+}$ estimate	RMSE $c_{\varepsilon 3+} = 1.0$ (standard case)	RMSE $c_{\varepsilon 3+}$ estimate
2009 direct case	2.1742	2.9521	0.2628
2009 normalized case	2.1917	1.6521	0.1333
2011 direct case	2.0876	4.0208	0.3109
2011 normalized case	2.0955	1.2987	0.0759

observations, 8-day mean satellite Chl *a* data of 2009 are used for the calibration. Figure 2 shows that in 2009, the observed bloom occurs about a month earlier compared to the true scenario of the ITE (Fig. 4). The observed surface Chl *a* has an immediate strong peak and concentrations decrease to prebloom values within 1.5 months, while the modeled surface Chl *a* increases steadily until June and then decreases within a month to a low value. Regardless of the discrepancies in shape and timing between the modeled and observed blooms, the values are generally of the same order.

In section 3b(2) the calibration to satellite surface Chl *a* is repeated for the year 2011 to test the sensitivity of the calibration result. Both datasets are first used directly for the calibration (*direct case*) and then the observations are normalized before they are used for the calibration (*normalized case*). The normalization is done by dividing the modeled and observed surface Chl *a* data by their corresponding maximum value. The modeled time series is still based on 12-hourly data, and OpenDA compares the measured and observed time series only after the normalization. This normalization is done to focus more on the shape and timing of the bloom than on the actual concentration of Chl *a*. At the end of each section, results are compared to ST observations. Table 4 gives an overview of the calibration results.

1) 2009 MODIS *AQUA* SATELLITE OBSERVATIONS

The 2009 satellite observations in Fig. 2 are available every 8 days and are directly read as observations into the calibration algorithm (direct case). For each iteration of the calibration, GOTM-NP is run from 1 January 2008 to 31 December 2009 with the new estimate for $c_{\varepsilon 3+}$. Figure 9a shows the results of four calibration steps of the direct case for 2009. The calibration is initialized with $c_{\varepsilon 3+} = 2$, which leads the occurrence of the main peak of the bloom in late April. An increase of $c_{\varepsilon 3+}$ reduces the late peak, increases the minor peak at the end of February, and shifts

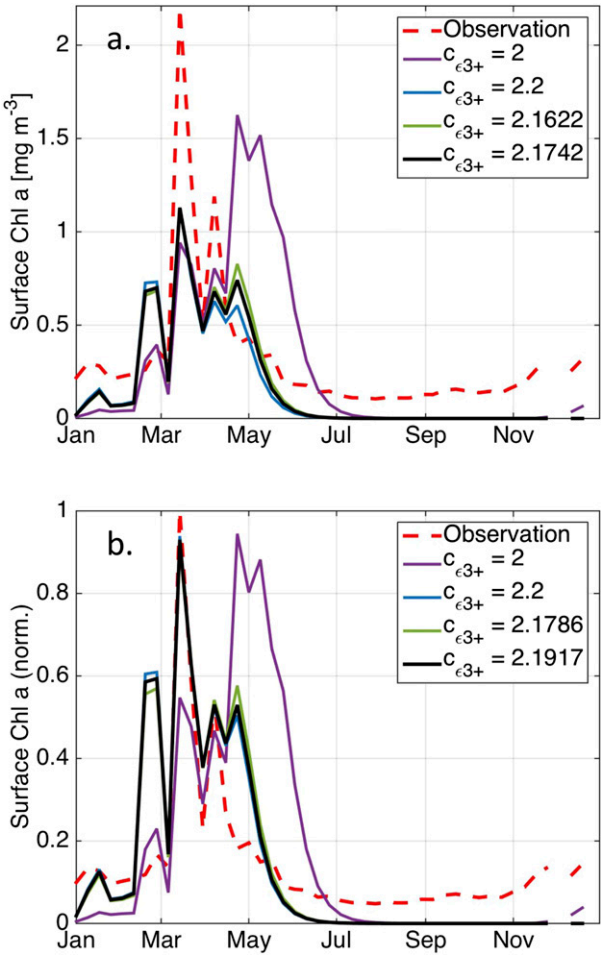

FIG. 9. Observations and model results of surface Chl *a* for (a) the direct case and (b) the normalized case based on MODIS *Aqua* Chl *a* and ECMWF forcing for the year 2009. The black line gives the best fit with minimum cost *S*.

the focus toward mid-March as in the observations. Even though the strength of the main peak is underestimated, the result based on the best fit ($c_{\varepsilon 3+} = 2.1742$) resembles the general characteristics of the satellite observations very well: the timing of the main peak agrees, and the main peak is preceded and followed by minor peaks. For the normalized case, Fig. 9b shows that the main peak is again well represented by the best fit, which has a slightly higher $c_{\varepsilon 3+}$ than the best fit of the direct case. The normalization brings model results of the main and the succeeding peak closer to the observations, while the preceding peak is overestimated. Table 4 shows that the calibration reduces the RMSE by a factor of 10 for both the direct and normalized cases.

To determine which calibration performs better, ST observations of 23 July 2009 are compared to modeled profiles averaged over a time window of 5 days before and after the day of the in situ observation (Fig. 10). By

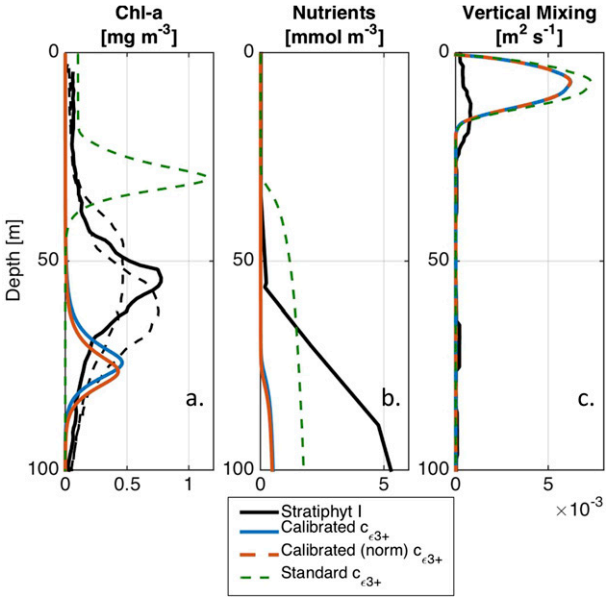

FIG. 10. Comparison of the GOTM-NP modeling results to ST observations on 23 Jul 2009 at 40.5°N, 13.2°W (solid black line). Vertical profiles are given for (a) Chl *a*, (b) nutrient concentration, and (c) vertical mixing. Model results are given for the standard parameterization ($c_{\varepsilon 3+} = 1.0$, dashed green line) and the two calibration results based on the MODIS *Aqua* 2009 data (blue and dashed red line). Model profiles are calculated as the mean over the five preceding and subsequent days of the main observation. The dashed black lines give the Chl *a* profiles on 22 Jul and 23 Jul at 39.5°N, 13.4°W and 41.2°N, 13.1°W, respectively. The extra profiles and the averaging of the model data serve to give a more generalized picture.

using the (time) average, the presented model state is not affected by variations on short time scales, which allows for focusing on the predominant state of the water column. Additionally, Chl *a* profiles of the two neighboring CTD measurements are plotted (observations of nutrients and vertical mixing are not available at these locations). In Fig. 10a, the main Chl *a* observation shows a well-defined DCM at about 55-m depth. The other two measured Chl *a* profiles vary in depth and intensity. The modeled Chl *a* profile based on the standard calibration ($c_{\varepsilon 3+} = 1.0$) shows a DCM around 30-m depth, while a low Chl *a* concentration is also present in the mixed layer, indicating a recent transition from a UCM. The new calibrations based on satellite data show a DCM at about 75-m depth, with the normalized calibration result being slightly deeper. It follows that while all model results cannot reproduce the depth of the measured DCM, the calibrations result in DCMs that are closer to the range of measurements, both in depth and intensity. Nutrient profiles (measured and modeled; Fig. 10b) reflect the characteristics of the Chl *a* profiles: The depth of the nutricline is found just below the Chl *a* maximum. Comparison of the vertical mixing profiles in Fig. 10c shows that the change in $c_{\varepsilon 3+}$ has only a small influence on the summer stratification (as was already seen in Fig. 6). Still, the calibrated $c_{\varepsilon 3+}$ reduces the strength of the mixing, thus bringing it closer to the observations.

Since $c_{\varepsilon 3+}$ is not applied in the model while the water column is stably stratified, only limited conclusions can be drawn from observations of a single day in summer. Therefore, Fig. 11 shows the full modeled year 2009 based on the new calibration with $c_{\varepsilon 3+} = 2.1742$ (direct case). Increasing $c_{\varepsilon 3+}$ strongly reduces winter mixing compared to the standard parameterization (Fig. 4d). While this provides fewer nutrients to the surface (Fig. 11c), it also allows for an earlier spring bloom by relaxing the light limitation and for concentrating the phytoplankton in a shallower mixed layer (Figs. 11a and 11b). Therefore, the new calibration brings the modeled surface Chl *a* concentration closer to the observed satellite data. In contrast to the standard model setup, the DCM is very distinctive after June and Chl *a* is very low from July to December. Only when the mixing deepens in winter is the DCM diluted in the mixed layer.

2) 2011 MODIS *AQUA* SATELLITE OBSERVATIONS

Satellite Chl *a* observations in Fig. 2 show that the surface Chl *a* peaked later in 2011 compared to 2009. Concentrations increased by late March and reached their maximum of 3.5 mg Chl *a* m^{-3} in early April. This peak is remarkably stronger than the one in 2009. Satellite data are again given as an 8-day mean. For the calibration, GOTM-NP is initialized with $c_{\varepsilon 3+} = 2$ on 31 December 2009 (of the equilibrium run) and run to the end of 2011. This provides one year of spinup before the 2011 data are used for the calibration with the DUD algorithm.

Figure 12a shows results of six calibration steps based on the direct case. All modeled surface Chl *a* data show a peak in early March similar to the observations. For low values of $c_{\varepsilon 3+}$, summer surface Chl *a* is high and maintained even until August. Increasing $c_{\varepsilon 3+}$ hardly affects the peak in March (except for $c_{\varepsilon 3+} = 2.2$), but it effectively reduces the summer Chl *a*. Even though modeled Chl *a* is higher compared to the 2009 model results, the strong peak of the observations is not reached.

The best fit of the normalized case has a slightly higher value of $c_{\varepsilon 3+}$ than the direct case, which mainly reduces the strength of the small peak in early May. As a consequence, the RMSE of the normalized case is reduced by 94% compared to the standard calibration of $c_{\varepsilon 3+}$, while the direct case leads to a slightly lower reduction (92.3%). Whether this is an improvement becomes visible in

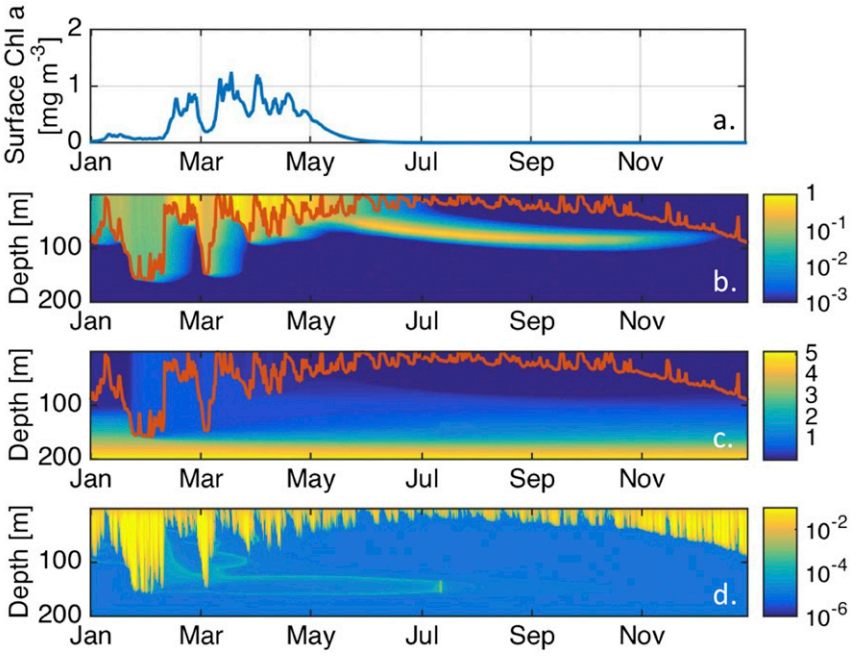

FIG. 11. As in Fig. 4, but calibrated model results with $c_{\varepsilon 3+} = 2.1742$ based on the MODIS *Aqua* 2009 surface Chl *a* observations (direct case).

the comparison to the ST observations of April 2011. Figure 13 reveals that the calibration to the normalized satellite data brings the modeled Chl *a* profile closer to the observations compared to the direct case and the standard parameterization. Still, all modeled values are higher than those in the observations. The comparison of the nutrient profiles is ambiguous (Fig. 13b): while the new calibration performs better in the mixed layer, nutrient levels are too low at depth. In fact, the new calibration leads to a strong reduction of nutrients at depth, while the standard calibration shows a rather homogeneous nutrient profile. Probably the most significant result is the vertical mixing profiles of the two calibration cases (Fig. 13c): The modeled and measured vertical mixing profiles are of the same order, and the MLD differs by only 5 m. The latter is also the case for the standard parameterization, but the modeled mixing in the mixed layer is twice as strong for the standard case compared to the in situ observations and the new calibration.

Figure 14 provides an overview of the whole modeled year 2011 based on the new calibration with $c_{\varepsilon 3+} = 2.0955$ (normalized case). Moderate winter mixing allows for an early Chl *a* bloom and provides simultaneously sufficient nutrients to the surface to sustain the growth. High background values of K_T in Fig. 1b suggest a recent deep mixing event (>100 m) that would agree with the modeled mixing in March (Fig. 14). As shown in Fig. 12, a further increase of $c_{\varepsilon 3+}$ causes an overall reduction of the Chl *a* intensity due to the lack of nutrients.

4. Summary, discussion, and conclusions

We developed a new general methodology to estimate parameters of the k–ε turbulence model in GOTM using only observations of surface Chl *a*. A nutrient–phytoplankton model (NP) was used to connect vertical mixing to surface Chl *a* concentrations. Both of these models are only one-dimensional vertical representations of the upper-ocean processes and hence neglect potential important effects of horizontal advection. The new method was tested using observations at one particular station in the North Atlantic for which extensive measurements were available such that the parameters in the NP model could be independently determined. To illustrate the method, we choose the parameter $c_{\varepsilon 3+}$ in the $k-\varepsilon$ model that weighs the contribution of the buoyancy production G to the dissipation rate of turbulent kinetic energy ε in unstably stratified situations. Changing $c_{\varepsilon 3+}$ mainly affects the depth of the winter mixing and the strength of the stratification.

Results of the identical twin experiments show that the model is very robust in terms of the experimental setup and that the performance of the method does not depend on the initial guess of $c_{\varepsilon 3+}$. Experiments with a number of noise amplitudes ($\sigma \in [0.005, 2.5]$ mg Chl *a* m^{-3})

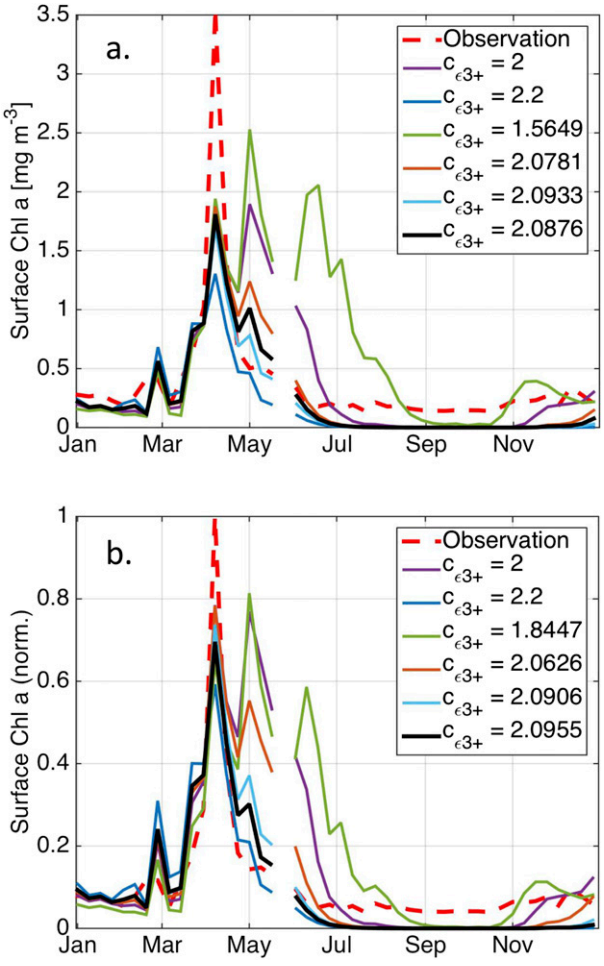

FIG. 12. Observations and model results of surface Chl *a* for (a) the direct case and (b) the normalized case based on MODIS *Aqua* Chl *a* and ECMWF forcing for the year 2011. The black line gives the best fit with minimum cost *S*.

to generate artificial observations showed that even with a noise $\sigma = 0.5\,\mathrm{mg\,Chl}\,a\,\mathrm{m}^{-3}$ (~25% of maximum Chl *a*), the calibrated $c_{\varepsilon 3+}$ value lies in close vicinity of the *true* value. In fact, the modeled surface Chl *a* based on this calibration example deviates only by $0.02\,\mathrm{mg\,Chl}\,a\,\mathrm{m}^{-3}$ from the true surface Chl *a*, which lies well below the applied noise. Results with different sampling frequencies (12-hourly to monthly data) and different sampling sequences (e.g., covering the whole or only parts of the bloom) show that as long as dominant features like the timing (onset and length) and the shape of the bloom are covered, the data can be used for the calibration of $c_{\varepsilon 3+}$.

Encouraged by these findings, the calibration method was applied to real observations of surface Chl *a* in the eastern North Atlantic for the years 2009 and 2011. Both years are characterized by a strong spring bloom and low surface Chl *a* during summer and fall. The choice of these two years and the location is motivated by in situ observations of the vertical mixing, as well as vertical profiles of Chl *a* and nutrients, which allow for validating the performance of the calibration method. The calibration to satellite data (*direct case)* yielded for both years a $c_{\varepsilon 3+}$ value that is significantly higher than its standard value. As a consequence, modeled winter mixing is effectively reduced and stratification is enhanced. These results are in better agreement with the observations, though the validation is limited by the sparse observations and their timing. Especially during the summer months when the water column is generally stable, the effect of $c_{\varepsilon 3+}$ on the modeled mixing is weak, since it affects only unstably stratified situations.

An additional calibration performed using normalized surface Chl *a* (normalized case) aims to reproduce the timing and shape of the bloom rather than the actual concentration of surface Chl *a*. Results show that the calibrated value of $c_{\varepsilon 3+}$ is slightly increased compared to the direct case for both years. In general, an increase of $c_{\varepsilon 3+}$ causes an earlier but weaker and shorter bloom. It follows that the *normalized case* yields a better result for the comparison with the spring 2011 Chl *a* profiles but a worse result for the comparison with the summer 2009 Chl *a* profiles. Still, differences in the mixing between the normalized and direct cases are very small and both results perform better than the standard calibration. We therefore suggest using normalized surface Chl *a* only if values of the measured and the modeled surface Chl *a* are far off, while the shape and timing of the growth cycle are in good agreement. Generally, the direct usage of the satellite data is a more robust choice, since it prevents unrealistic values of the modeled surface Chl *a*.

The aim of this work was to use remotely sensed Chl *a* data to estimate properties of upper-ocean vertical mixing. The results presented show that the method performs well for different years at one location, but how applicable is it to other locations? A successful calibration requires a biological model that is capable of representing the dominant growth dynamics at the given location. Here, biological and optical parameters were previously calibrated to the ST observations of summer 2009 (Hahn-Woernle et al. 2014). The station is characterized by light limitation due to deep mixing in winter, a UCM with the onset of stratification in spring, and a DCM due to nutrient limitation in summer. Preliminary tests have shown that neighboring measurement stations of the ST cruise (e.g., at 44.3°N, 12.6°W) that have the same growth characteristics lead to similar calibration results. This suggests that the current GOTM-NP model setup could be used over a latitudinal

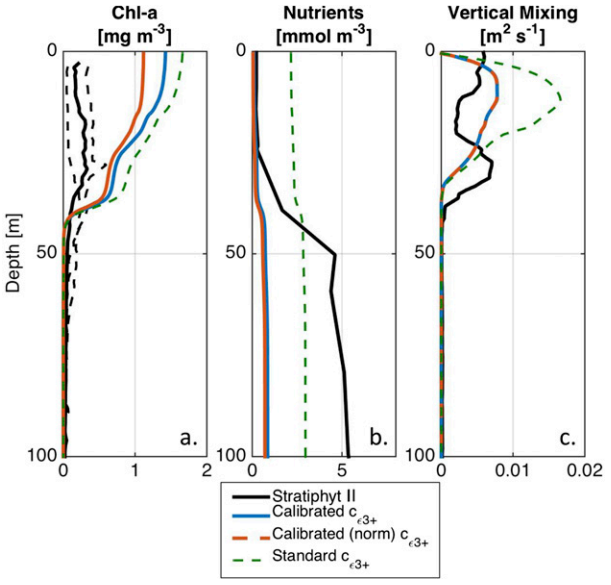

FIG. 13. As in Fig. 10, but comparing GOTM-NP modeling results to ST observations on 18 Apr 2011 at 40.5°N, 13.2°W (solid black line). The dashed black lines give the Chl *a* profiles on 17 Apr and 18 Apr at 39.5°N, 13.4°W and 41.2°N, 13.1°W, respectively.

band of 5° width, taking changes in the deep nutrient concentration (N_{Zb}) into account. Applying the calibration method to locations with different growth characteristics requires a new calibration to in situ data. Following the calibration method presented by Hahn-Woernle et al. (2014), in situ profiles of vertical mixing, Chl *a*, nutrients, and, preferably, light during a characteristic stage of the growth (here a DCM in summer) would be necessary. Even though every new calibration raises the need for further observations, the application to satellite data of 2011 shows that once the model is calibrated, it can also be applied to other years. Additionally and more generally, the results presented here show that surface Chl *a* is very sensitive to changes in $c_{\varepsilon 3+}$ and thereby to changes in the vertical mixing, even on very small scales. This result on its own is very encouraging for continuing further research with other, possibly more realistic biological models.

Rodi (1987) states that the value of $c_{\varepsilon 3}$ has been found to depend on the flow situation. Therefore, he differentiates $c_{\varepsilon 3}$ between stable ($G \leq 0$) and unstable ($G > 0$) stratification by choosing $c_{\varepsilon 3-}$ (close to 0) and $c_{\varepsilon 3+}$ (equal to 1), respectively. Still, he appeals for further research on the value of $c_{\varepsilon 3}$ and it has been matter of discussion in numerous works. Baumert and Peters (2000) give an overview of values used in different realizations of the k–ε model and the Mellor–Yamada model (Mellor and Yamada 1974) that range between −1.4 (Burchard and Baumert 1995) and 1.45 (Haroutunian and Launder 1988). Most of these values, as well as $c_{\varepsilon 3} = -1.4$ derived by Baumert and Peters (2000), are valid for stable, neutral, and weakly unstable stratification. Applying a negative value to the unstable case (e.g., $c_{\varepsilon 3+} = -1.0$) in our setup leads to even stronger winter mixing and consequently a worse representation of the (ST) site in the eastern North Atlantic. Our findings therefore suggest that the unstable state should be parameterized by a positive $c_{\varepsilon 3+}$ (as suggested by Rodi 1987) with a value of $c_{\varepsilon 3+}$ in the interval [2.0, 2.2].

In situ or laboratory measurements of, for example, temperature, velocity, or oceanic microstructure data, are often used to empirically determine the parameters of the turbulence model (Rodi 1987; Baumert and Peters 2000; Zhang et al. 2015). The results presented in this work show that surface Chl *a* is an effective indicator for upper-ocean vertical mixing and stratification. The key advantage of using surface Chl *a* data lies in the long-term effect that the enhanced nutrient supply caused by deep mixing events has on the phytoplankton growth (cf. Fig. 6). Under the same stratified conditions in spring and early summer, phytoplankton blooms vary in intensity and timing due to differences in the preceding winter mixing. It is therefore demonstrated, to our knowledge for the first time, that surface Chl *a* can be used for the calibration of parameters in turbulence models. We hope that this methodology is applied to future ocean models to improve the modeled representation of upper-ocean turbulent flows and their effect on phytoplankton.

Acknowledgments. We thank Dr. Werner Kramer at Vortech B. V., Delft, the Netherlands, for his valuable support with the OpenDA software. This work was funded by the NSO User Support Programme under Grant ALW-GO-AO/11-08 through the COLOURMIX project with financial support from the Netherlands Organization for Scientific Research (NWO). We thank the NASA Ocean Biology (OB.DAAC) group for making the MODIS *Aqua* R2014.0 ocean color data available (downloaded 11 December 2015, http://oceancolor.gsfc.nasa.gov).

APPENDIX A

The k–ε Model in GOTM

A general variable—say, ψ—describing a turbulent field can be decomposed into a mean and a fluctuating part: $\psi = \langle\psi\rangle + \psi'$. To simplify the notation, mean flow variables like salinity S, potential temperature Θ, buoyancy B, and pressure P, as well as the mean horizontal velocity field (U, V), are written in capital letters instead of using $\langle\cdot\rangle$. All state variables are assumed to be horizontally

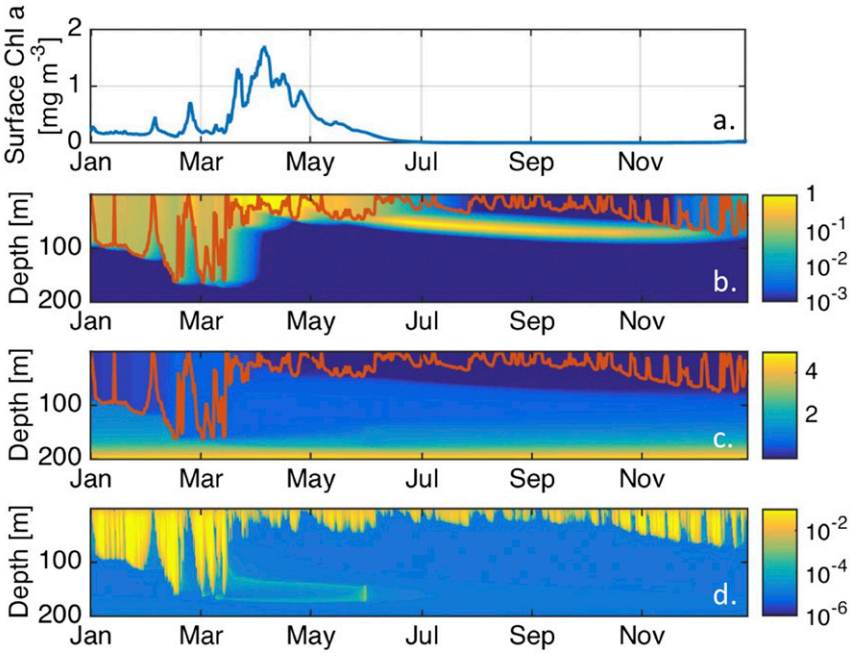

FIG. 14. As in Fig. 4, but calibrated model results with the best fit for $c_{\varepsilon 3+} = 2.0955$ based on the normalized 2011 MODIS *Aqua* surface Chl *a* (normalized case).

homogeneous. Balances for S and Θ, and transport equations for U, V and B are defined as follows:

$$\frac{DS}{Dt} = \mathscr{D}_S, \tag{A1}$$

$$\frac{D\Theta}{Dt} = \mathscr{D}_T + \frac{1}{C_p \rho_0}\frac{\partial I_{\mathrm{SWR}}(z)}{\partial z}, \tag{A2}$$

$$\frac{DU}{Dt} = \mathscr{D}_U + \int_z^0 \frac{\partial B}{\partial x} dz' - C_f U\sqrt{U^2+V^2}, \tag{A3}$$

$$\frac{DV}{Dt} = \mathscr{D}_V + \int_z^0 \frac{\partial B}{\partial y} dz' - C_f V\sqrt{U^2+V^2}, \tag{A4}$$

$$\frac{\partial P}{\partial z} + g\langle\rho\rangle = 0, \tag{A5}$$

$$B = -g\frac{\langle\rho\rangle - \rho_0}{\rho_0}, \tag{A6}$$

where C_p is the heat capacity of seawater, and ρ_0 is the reference density and C_f is a friction coefficient. The shortwave radiation $I_{\mathrm{SWR}}(z)$ is an internal source of heat computed according to the exponential law (Paulson and Simpson 1977)

$$I_{\mathrm{SWR}}(z) = I_{\mathrm{SWR}}(0)[Ae^{z/\eta_1} + (1-A)e^{z/\eta_2}]B_d(z), \tag{A7}$$

where A (0.58) is the nonvisible part of the incoming shortwave radiation $I_{\mathrm{SWR}}(0)$, the absorption coefficients η_1 and η_2 depend on the water type, and $B_d(z)$ is the biological damping term. Biological damping is not considered for the balance of heat, but for the light profile in the biological model (cf. section 2c).

Atmospheric fluxes

The total surface heat flux Q_{tot} is given by the sum of the latent heat flux Q_e, the sensible heat flux Q_h, and the longwave back radiation Q_b:

$$Q_{\mathrm{tot}} = Q_e + Q_h + Q_b. \tag{A8}$$

The back radiation is calculated according to Clark (1974) as

$$Q_b = -[s\sigma\Theta_s^4(0.39 - 0.050\sqrt{e_a})(1 - k_j C^2) + 4s\sigma\Theta_s^3(\Theta_s - \Theta_a)], \tag{A9}$$

where s is the ratio of the sea surface radiation to a blackbody; σ is the Stefan–Boltzmann constant; Θ_s and Θ_a are the sea surface and air temperature (°C), respectively; e_a is the vapor pressure (mb); k_j is a function of latitude (Johnson et al. 1965); and C is the cloudiness in tenths of celestial dome covered.

According to the Kondo (1975) bulk formulas, first the transfer coefficients of the surface fluxes (c_{dd}, c_{ed}, and c_{hd}) are determined based on Θ_s, Θ_a and the observed wind vector at 10-m height (W_x, W_y). Then, Q_e, Q_h and the surface momentum flux vector (τ_x^s, τ_y^s) are

determined, taking additionally the air pressure at 2 m and the relative humidity (here derived from the dew-point temperature) into account:

$$\begin{aligned}\tau_x^s &= c_{dd}\rho_a W_x W_{SS},\\ \tau_y^s &= c_{dd}\rho_a W_y W_{SS},\\ Q_e &= c_{ed}L\rho_a W_{SS}(q_s - q_a),\\ Q_h &= c_{hd}C_{pa}\rho_a W_{SS}(\Theta_s - \Theta_a),\end{aligned} \tag{A10}$$

where the average value of the wind speed relative to the sea surface is given by $W_{SS} = (W_x^2 + W_y^2)^{1/2}$, the specific evaporation heat of seawater is given by L, and the specific and actual saturation humidities are given by q_s and q_a, respectively.

APPENDIX B

The NP Model

In the NP model, only the photosynthetic active part I_{in} of the incoming shortwave radiation, I_{SWR} is taken into account:

$$I_{in} = (1 - A)I_{SWR}(0), \tag{B1}$$

where A (0.58) is the nonvisible part of I_{SWR} (Jerlov 1968). Incoming PAR I_{in} and the vertical mixing ν_t^B are updated within GOTM at every time step.

In Eq. (11), the minimum photosynthetic active radiation I_{min} is a new element compared to the original model calibrated by Hahn-Woernle et al. (2014). The calibration was done under constant daily mean light conditions. In GOTM, light follows the daily cycle. A comparison of GOTM-NP and original NP model results under the same forcing has shown that only with the introduction of I_{min} and an increased growth rate μ_{max}, the original NP model results could be reproduced by the GOTM-NP model.

APPENDIX C

OpenDA Calibration Procedure

The calibration is started with an unperturbed run and one sensitivity run. Let λ_I and λ_{II} be the first two parameter estimates, and their corresponding function values $f(x_I;\lambda_I)$ and $f(x_{II};\lambda_{II})$ are stored in memory. The parameters are sorted according to their cost function $S(\lambda)$ with λ_I having the higher cost function and λ_{II} having the lower cost function.

The new parameter estimate λ^* is based on λ_{II}, the difference between the two best estimates ($\Delta\lambda = \lambda_I - \lambda_{II}$), and a parameter α^*:

$$\lambda^* = \lambda_{II} + \Delta\lambda\alpha^*. \tag{C1}$$

To determine α^*, a linear approximation of the predictions l is defined as

$$l(\alpha^*) = f(x_{II};\lambda_{II}) + \Delta F\alpha^*, \tag{C2}$$

where ΔF is given by $\Delta F = f(x_I;\lambda_I) - f(x_{II};\lambda_{II})$.

Minimizing S for $l(\alpha^*)$ [instead of $f(x;\lambda)$] leads to

$$\alpha^* = (\Delta F'\Delta F)^{-1}\Delta F'[y - f(x_{II};\lambda_{II})]. \tag{C3}$$

If $S(\lambda^*)$ is less than $S(\lambda^I)$, then λ_I is replaced by λ_*, and the two estimates are again sorted according to their corresponding cost function. If $S(\lambda^*)$ is not less than $S(\lambda^I)$, then a line search is done along the direction λ_{II} to λ^*:

$$\lambda^* = \lambda_{II} + \delta(\lambda^* - \lambda_{II}). \tag{C4}$$

The step size $\delta \in \Re$ is iteratively reduced according to

$$\delta_i = \begin{cases} 1 & i = 0 \\ \beta^* \times (1/2)^i & i = 1,\ldots,m \end{cases}$$

until a λ^* is reached for which $S(\lambda^*)$ is less than $S(\lambda_{II})$, if that exists. The parameter $\beta^* = \pm 1$ determines whether the search is continued in a positive or negative direction and depends on the setup. Here, a negative search is initiated for $i > 3$. The procedure is stopped as soon as one of the stopping criteria is fulfilled (e.g., $i = m$, with m being the prescribed maximum number of iterations). The best fit will be given by the final value of λ_{II} with the lowest cost S.

REFERENCES

Allen, J., J. Siddorn, J. Blackford, and F. Gilbert, 2004: Turbulence as a control on the microbial loop in a temperate seasonally stratified marine systems model. *J. Sea Res.*, **52**, 1–20, doi:10.1016/j.seares.2003.09.004.

Baumert, H., and H. Peters, 2000: Second-moment closures and length scales for weakly stratified turbulent shear flows. *J. Geophys. Res.*, **105**, 6453–6468, doi:10.1029/1999JC900329.

Behrenfeld, M. J., and E. S. Boss, 2014: Resurrecting the ecological underpinnings of ocean plankton blooms. *Annu. Rev. Mar. Sci.*, **6**, 167–194, doi:10.1146/annurev-marine-052913-021325.

Burchard, H., and H. Baumert, 1995: On the performance of a mixed-layer model based on the *k*-ε turbulence closure. *J. Geophys. Res.*, **100**, 8523–8540, doi:10.1029/94JC03229.

——, and O. Petersen, 1999: Models of turbulence in the marine environment—A comparative study of two-equation turbulence models. *J. Mar. Syst.*, **21**, 29–53, doi:10.1016/S0924-7963(99)00004-4.

——, and K. Bolding, 2001: Comparative analysis of four second-moment turbulence closure models for the oceanic mixed layer. *J. Phys. Oceanogr.*, **31**, 1943–1968, doi:10.1175/1520-0485(2001)031<1943:CAOFSM>2.0.CO;2.

Canuto, V., A. Howard, Y. Cheng, and M. Dubovikov, 2001: Ocean turbulence. Part I: One-point closure model—Momentum and

heat vertical diffusivities. *J. Phys. Oceanogr.*, **31**, 1413–1426, doi:10.1175/1520-0485(2001)031<1413:OTPIOP>2.0.CO;2.

Clark, N. E., L. Eber, R. M. Laurs, J. A. Renner, and J. F. T. Saur, 1974: Heat exchange between ocean and atmosphere in the eastern North Pacific for 1961-1971. NOAA Tech. Rep. NMFS SSRF-682, 108 pp.

Dee, D. P., and Coauthors, 2011: The ERA-Interim reanalysis: Configuration and performance of the data assimilation system. *Quart. J. Roy. Meteor. Soc.*, **137**, 553–597, doi:10.1002/qj.828.

Fofonoff, R., and R. C. Millard, 1983: Algorithms for the computation of fundamental properties of seawater. UNESCO Tech. Papers in Marine Science 44, UNESCO, 54 pp.

Hahn-Woernle, L., H. A. Dijkstra, and H. J. van der Woerd, 2014: Sensitivity of phytoplankton distributions to vertical mixing along a North Atlantic transect. *Ocean Sci.*, **10**, 993–1011, doi:10.5194/os-10-993-2014.

Haroutunian, V., and B. E. Launder, 1988: Second-moment modelling of free buoyant shear flows: A comparison of parabolic and elliptic solutions. *Stably Stratified Flow and Dense Gas Dispersion*, J. S. Puttock, Ed., Institute of Mathematics and Its Applications Conference Series, Vol. 15, Oxford University Press, 409–430.

Huisman, J., and B. Sommeijer, 2002: Population dynamics of sinking phytoplankton in light-limited environments: Simulation techniques and critical parameters. *J. Sea Res.*, **48**, 83–96, doi:10.1016/S1385-1101(02)00137-5.

——, P. van Oostveen, and F. J. Weissing, 1999: Species dynamics in phytoplankton blooms: Incomplete mixing and competition for light. *Amer. Nat.*, **154**, 46–68, doi:10.1086/303220.

Jerlov, N., 1968: *Optical Oceanography*. Elsevier Oceanography Series, Vol. 5, Elsevier, 194 pp.

Johnk, K. D., J. Huisman, J. Sharples, B. Sommeijer, P. M. Visser, and J. M. Stroom, 2008: Summer heatwaves promote blooms of harmful cyanobacteria. *Global Change Biol.*, **14**, 495–512, doi:10.1111/j.1365-2486.2007.01510.x.

Johnson, J., G. Flittner, and M. Cline, 1965: Automatic data processing program for marine synoptic radio weather reports. Special Scientific Report—Fisheries, U.S. Department of the Interior, Bureau of Commercial Fisheries 503, 74 pp.

Jurado, E., H. A. Dijkstra, and H. J. van der Woerd, 2012a: Microstructure observations during the spring 2011 STRATIPHYT-II cruise in the northeast Atlantic. *Ocean Sci.*, **8**, 945–957, doi:10.5194/os-8-945-2012.

——, H. J. van der Woerd, and H. A. Dijkstra, 2012b: Microstructure measurements along a quasi-meridional transect in the northeastern Atlantic Ocean. *J. Geophys. Res.*, **117**, C04016, doi:10.1029/2011JC007137.

Klausmeier, C., and E. Litchman, 2001: Algal games: The vertical distribution of phytoplankton in poorly mixed water columns. *Limnol. Oceanogr.*, **46**, 1998–2007, doi:10.4319/lo.2001.46.8.1998.

Kondo, J., 1975: Air-sea bulk transfer coefficients in diabatic conditions. *Bound.-Layer Meteor.*, **9**, 91–112, doi:10.1007/BF00232256.

Levitus, S., J. Antonov, T. Boyer, and C. Stephens, 2000: Warming of the world ocean. *Science*, **287**, 2225–2229, doi:10.1126/science.287.5461.2225.

Mellard, J. P., K. Yoshiyama, E. Litchman, and C. A. Klausmeier, 2011: The vertical distribution of phytoplankton in stratified water columns. *J. Theor. Biol.*, **269**, 16–30, doi:10.1016/j.jtbi.2010.09.041.

Mellor, G. L., and T. Yamada, 1974: A hierarchy of turbulence closure models for planetary boundary layers. *J. Atmos. Sci.*, **31**, 1791–1806, doi:10.1175/1520-0469(1974)031<1791:AHOTCM>2.0.CO;2.

Mojica, K. D. A., and Coauthors, 2015: Phytoplankton community structure in relation to vertical stratification along a north-south gradient in the Northeast Atlantic Ocean. *Limnol. Oceanogr.*, **60**, 1498–1521, doi:10.1002/lno.10113.

Moore, L. R., and S. W. Chisholm, 1999: Photophysiology of the marine cyanobacterium Prochlorococcus: Ecotypic differences among cultured isolates. *Limnol. Oceanogr.*, **44**, 628–638, doi:10.4319/lo.1999.44.3.0628.

Olbert, A. I., S. Nash, E. Ragnoli, and M. Hartnett, 2014: Parameterization of turbulence models using 3DVAR data assimilation. *Proc. 11th Int. Conf. on Hydroinformatics (HIC 2014)*, New York, NY, City University of New York, 173. [Available online at http://academicworks.cuny.edu/cc_conf_hic/173/.]

Osborn, T., and C. S. Cox, 1972: Oceanic fine structure. *Geophys. Fluid Dyn.*, **3**, 321–345, doi:10.1080/03091927208236085.

Paulson, C., and J. Simpson, 1977: Irradiance measurements in upper ocean. *J. Phys. Oceanogr.*, **7**, 952–956, doi:10.1175/1520-0485(1977)007<0952:IMITUO>2.0.CO;2.

Ralston, M., and R. Jennrich, 1978: DUD, a derivative-free algorithm for nonlinear least squares. *Technometrics*, **20**, 7–14, doi:10.1080/00401706.1978.10489610.

Rodi, W., 1987: Examples of calculation methods for flow and mixing in stratified fluids. *J. Geophys. Res.*, **92**, 5305–5328, doi:10.1029/JC092iC05p05305.

Ryabov, A., L. Rudolf, and B. Blasius, 2010: Vertical distribution and composition of phytoplankton under the influence of an upper mixed layer. *J. Theor. Biol.*, **263**, 120–133, doi:10.1016/j.jtbi.2009.10.034.

Schlitzer, R., 2002: Interactive analysis and visualization of geoscience data with ocean data view. *Comput. Geosci.*, **28**, 1211–1218, doi:10.1016/S0098-3004(02)00040-7.

Schumann, U., and T. Gerz, 1995: Turbulent mixing in stably stratified shear flows. *J. Appl. Meteor.*, **34**, 33–48, doi:10.1175/1520-0450-34.1.33.

Umlauf, L., and H. Burchard, 2005: Second-order turbulence closure models for geophysical boundary layers. A review of recent work. *Cont. Shelf Res.*, **25**, 795–827, doi:10.1016/j.csr.2004.08.004.

van de Poll, W. H., and Coauthors, 2013: Phytoplankton chlorophyll *a* biomass, composition, and productivity along a temperature and stratification gradient in the northeast Atlantic Ocean. *Biogeosciences*, **10**, 4227–4240, doi:10.5194/bg-10-4227-2013.

Waterhouse, A. F., and Coauthors, 2014: Global patterns of diapycnal mixing from measurements of the turbulent dissipation rate. *J. Phys. Oceanogr.*, **44**, 1854–1872, doi:10.1175/JPO-D-13-0104.1.

Yu, L., and J. Obrien, 1991: Variational estimation of the wind stress drag coefficient and the oceanic eddy viscosity profile. *J. Phys. Oceanogr.*, **21**, 709–719, doi:10.1175/1520-0485(1991)021<0709:VEOTWS>2.0.CO;2.

Zhang, X., G. Han, D. Li, X. Wu, W. Li, and P. C. Chu, 2015: Variational estimation of wave-affected parameters in a two-equation turbulence model. *J. Atmos. Oceanic Technol.*, **32**, 528–546, doi:10.1175/JTECH-D-14-00087.1.